Journal of Environmental Chemical Engineering 9 (2021) 106191

Contents lists available at ScienceDirect

Journal of Environmental Chemical Engineering

journal homepage: www.elsevier.com/locate/jece

Facile utilization of magnetic MnO_2@Fe_3O_4@sulfonated carbon sphere for selective removal of hazardous Pb(II) ion with an excellent capacity: Adsorption behavior/isotherm/kinetic/thermodynamic studies

Panya Maneechakr *, Surachai Karnjanakom *

Department of Chemistry, Faculty of Science, Rangsit University, Pathumthani 12000, Thailand

ARTICLE INFO

Editor: Dr. GL Dotto

Keywords:
Carbon sphere
Pb^{2+} ion
Magnetic adsorbent
Adsorption behavior
Removal

ABSTRACT

Magnetic MnO_2@Fe_3O_4@sulfonated carbon sphere (CS-S-Fe-Mn) was used as a magnetic adsorbent for selective removal of Pb^{2+} ion from aqueous solution via co-creation between electrostatic force along with co-ordinate covalent bond. The CS-S-Fe-Mn was prepared via hydrothermal carbonization/sulfonation and followed by facile precipitation processes. The physical and chemical properties of CS-S-Fe-Mn and other adsorbents were characterized by BET-BJH, XRD, FTIR, VSM, SEM-EDS, pH_{pzc} and Boehm titration techniques. As observed, the CS-S-Fe-Mn exhibited a spherical (petal-like walls) shape with a good dispersion of Fe_3O_4 and MnO_2 particles, which had surface area of 146 m^2/g, total acidity-basicity of 7.87 mmol/g and negative surface charge ($pH < pH_{pzc}$). The paramagnetic properties of CS-S-Fe-Mn was well found with a saturation magnetization value of 21.8 emu/g, resulting in facile separation from water system using an external magnetic field. A maximum adsorption capacity (q_{max}) of Pb^{2+} over CS-S-Fe-Mn was 147.76 mg/g which had higher performance than previous references, resulting from synergetic effects of oxygen containing functional groups such as -C═O/C-O, -COOH and $-SO_3H$ as well as MnO_2. Moreover, the adsorption behaviors of Pb^{2+} onto CS-S-Fe-Mn were in good agreement with rapid monolayer-physisorption (E = 2.93 kJ/mol)/spontaneous-endothermic (ΔH = 49.12 kJ/mol) nature processes as well as intra-particle diffusion via two step mechanisms, supporting by isotherm, kinetic, thermodynamic and Weber-Morris models. This research provided a handy strategy for Pb^{2+} removal with high adsorption capacity from environmental wastewater.

1. Introduction

Discharging of untreated wastewater from metallurgical, tanneries and textile industries/mines is a serious problem of environmental pollution that needs to be considered in current state [1,2]. Lead (Pb) is one of most hazardous heavy metals which may be possibly existed in the human body via food chain or drinking water, leading to facile carcinogenicity [3,4]. The concentration of Pb^{2+} ion in drinking water should not exceed about 10 μg/L which is specified by World Health Organization (WHO) [5]. To offer a progressive environment with better quality of life, many researchers have been endeavored to develop the separation techniques such as membrane separation, ion exchange, chemical precipitation, adsorption and electrolysis deposition [6–10]. So far, the adsorption can be considered as a most promising technique for real application in wastewater treatment with the presence of heavy metals due to its eco-friendly, low operation cost, high capability for heavy metal removal [11,12]. Several adsorbent materials such as montmorillonite, biochar, chitosan, activated sludge and MOF have been applied for selective adsorption of Pb^{2+} from aqueous solution. Wang et al. [13] prepared 3D reticular-structured montmorillonite hydrogel for Pb^{2+} adsorption. They found that Pb^{2+} adsorption capability of 90 mg/g was well achieved, controlling by the amount of adsorption sites on montmorillonite hydrogel. Biochar prepared from pyrolysis of cotton straw was utilized for selective removal of Pb^{2+} in aqueous solution, and the results found that a maximum adsorption capacity of Pb^{2+} was 124.7 mg/g using biochar at pyrolysis temperature of 600 ℃ with a pH value of 5.5 [14]. Ahmed et al. [15] improved the biochar efficiency via H_2O_2 treatment process for Pb^{2+} removal. The number of oxygen functional groups on biochar was increased after oxidation by H_2O_2, leading to significant increasing of Pb^{2+} adsorption capacity (60.87 mg/g). Chen et al. [16] reported that selectivity of Pb^{2+} adsorption was well enhanced via electrostatic action between nitrogen

* Corresponding authors.
E-mail addresses: panya.m@rsu.ac.th (P. Maneechakr), surachai.ka@rsu.ac.th (S. Karnjanakom).

https://doi.org/10.1016/j.jece.2021.106191
Received 27 July 2021; Received in revised form 4 August 2021; Accepted 7 August 2021
Available online 10 August 2021

and oxygen groups in ninhydrin-functionalized chitosan. Veenhuyzen et al. [17] found that Pb^{2+} adsorption efficiency could be greatly improved over waste sludge chemically activated with $ZnCl_2$, resulting in the presence of high surface area and porosity. The Zr-MOF grafting by S, O and N functional groups also applied as adsorbent for the target pollutants such Pb^{2+} heavy metal [18]. Matsukevich et al. [19] achieved the excellent capacity up to 2989 mg/g for Pb^{2+} adsorption over magnesium oxide-nanocomposites material.

Unfortunately, even though these adsorbents show the high performance for Pb^{2+} removal, but they are still difficult to be separated them from aqueous solution using filtration or centrifugation technique which is required high operation cost and long operation time. Magnetic (Fe_3O_4) particle/adsorbent can be considered as a good choice to solve such above problems since it has high surface area with good physiochemical properties for metal adsorption, can be also easily separated by an exterior magnetic field [20]. Anywise, the direct utilization of pristine magnetic adsorbent may be inappropriate due to its slight capacity for metal removal, resulting from low surface area/unabundant of active site as well as its stability in form of ionic structure without assistant of covalent bond. Thus, the synergistic integration between magnetic with other active adsorbent can be considered as an interesting way for this research field. Recently, PANI@APTS-magnetic attapulgite composites is developed via co-precipitation method, and applied for selective adsorption of heavy metal ions. Zhang et al. [21] studied the preparation method of magnetized activated carbon via activating-pyrolyzing-magnetizing process. Nata et al. [22] reported that amine-rich functionalized magnetic adsorbent was not only give an easy recovery, but also exhibited high efficiency for selective adsorption of Pb^{2+} from environmental wastewater. Xu et al. [23] decorated the tetraethylenepentamine and graphene oxide onto surface of $MnFe_2O_4$ magnetic, and the results found that its surface area and porosity were increased to some extent while abundant amino and oxygen-containing functional groups were detected, leading to high enhancement for removal performance. Valenzuela et al. [24] found that Pb^{2+} and other heavy metals could be well removed using magnetic iron-modified calcium silicate hydrate via chemisorption mechanisms with assistance of ion exchange and salt formation. Based on above furtherance results, some undesired objectives are still required such as high production cost as well as complex preparation process.

In this research, we developed the magnetic MnO_2@Fe_3O_4@sulfonated carbon sphere (CS-S-Fe-Mn) for effective removal of Pb^{2+} with high adsorption capacity. Carbon sphere (CS) can be produced from biomass-derived carbohydrates via hydrothermal carbonization process under a series reaction including hydrolysis, deoxygenation, aromatization and polymerization at lower temperature around 180 ℃, comparing with traditional carbonization at higher temperatures of 500–600 ℃ [25]. Advantages of this process are energy saving along with carbon emission reduction. Owing to incomplete carbonization, the modification of desired active sites can be easily performed since abundant oxygen functional groups such as C–O/C═O, COOH and O-H are existed on CS surface, leading to strong enhancement for adsorption efficiency. Recently, Xu et al. [26] achieved the CS application derived from hydrothermal synthesis of glucose with sodium dodecylbenzene sulfonate for chromium removal process. Xu et al. [27] found that the efficient removal of mercury was well achieved by using MnO_2@CS material. Up to date, the investigations on Pb^{2+} adsorption over CS are quite scant. Here, the CS-S-Fe-Mn adsorbent was prepared and modified via hydrothermal carbonization/sulfonation processes and followed by precipitation of Fe_3O_4 and MnO_2. The physical-chemical properties of adsorbents were characterized by BET-BJH, XRD, FTIR, VSM, SEM-EDS, pH_{pzc} and Boehm titration techniques. The roles of each adsorbent before and after modification were discussed in details of Pb^{2+} adsorption behaviors. The various influences such as pH values, initial concentration of Pb^{2+}, contact time, and temperature were systematically investigated, supporting by Langmuir, Freundlich, Dubinin-Radushkevich, Temkin, Toth and Redlich-Peterson isotherms, kinetic and thermodynamic models. To the best of our knowledge, this research is not only provided the novel strategy/concept for facile preparation of redemptive adsorbent but also presented the adsorption behaviors and effective removal of Pb^{2+} ion from aqueous solution.

2. Experimental

2.1. Adsorbent preparation

(I) For preparation process of carbon sphere (CS), 5.0 g of sucrose was mixed with 30 mL of distilled water, and continuously stirred to obtain the transparent solution. The obtained solution was further transferred to autoclave reactor with a size of 50 mL, and heated at 180 ℃ for 16 h. It should be noted that the experimental conditions with a highest yield of CS for hydrothermal carbonization process were fixed based on our preliminary studies (Figs. S1-S3). Thereafter, black precipitate or CS was separated from mixture solution by filtration technique. Finally, it was washed with distilled water for several times to remove some impurities, and dried at 105 ℃ for overnight.

(II) For preparation process of sulfonated carbon sphere (CS-S), the certain amounts of CS and conc. H_2SO_4 were mixed at a ratio of CS to H_2SO_4 (1:3 g/mL), and followed by adding the distilled water until a solution volume of 30 mL was obtained. It should be noted that the optimum ratio with a highest acidity for hydrothermal sulfonation process was selected based on our preliminary studies (Fig. S4). The mixture solution was then transferred to autoclave reactor with a size of 50 mL, and heated at 180 ℃ for 10 h. Thereafter, CS-S was separated by filtration technique, and washed with distilled water for several times until neutral pH in washing water was detected. Finally, it was dried at 105 ℃ for overnight.

(III) For preparation process of Fe_3O_4@sulfonated carbon sphere (CS-S-Fe), 1.0 g of CS-S was sonicated in iron solution at a ratio of $2Fe^{3+}$ to $1Fe^{2+}$ with a concentration of 0.1 mol/L, consisting of $FeCl_3$ (53 mL) and $FeCl_2$ (27 mL) for 10 min. Then, 40 mL of ammonia solution was tardily dropped into mixture, and continuously sonicated for 10 min. During this step, Fe_3O_4 nanoparticles were grew up and enveloped on CS-S surface through co-precipitation of Fe^{3+} and Fe^{2+} ions. Finally, CS-S-Fe was easily separated by external magnetic field, washed with distilled water for several times to remove some impurities, and dried at 105 ℃ for overnight.

(IV) For preparation process of magnetic MnO_2@Fe_3O_4@sulfonated carbon sphere (CS-S-Fe-Mn), 1.0 g of CS-S-Fe was mixed in 25 mL of KMnO4 solution at a concentration of 0.04 mol/L, and stirred at 60 ℃ for 4 h [28]. During this step, MnO_2 nanoparticles grew up and enveloped on CS-S-Fe surface. Finally, CS-S-Fe-Mn was easily separated by external magnetic field, washed with distilled water for several times to remove some impurities, and dried at 105 ℃ for overnight. For comparison, pure MnO_2 was synthesized via hydrothermal precipitation method [29]. The synthesis steps of CS-S-Fe-Mn are summarized as shown in Fig. 1.

2.2. Adsorbent characterization

The details of BET-BJH, XRD, FTIR, VSM, SEM-EDS, pH_{pzc} and Boehm titration techniques are given in Supporting Information (SI) [30,31].

2.3. Bath adsorption test

To access the adsorption behaviors of Pb^{2+} onto various adsorbents as well as adsorption isotherm/kinetic/thermodynamic processes, batch experiments were carried out in conical flask size of 125 mL. A stock solution of Pb^{2+} at a concentration of 1000 mg/L was prepared from aqueous solution between $Pb(NO_3)_2$ before further dilution. In a typical process, 0.1 g of adsorbent was mixed in 25 mL of lead solution, and shaken at temperature of 303 K for 30 min with an agitation speed of

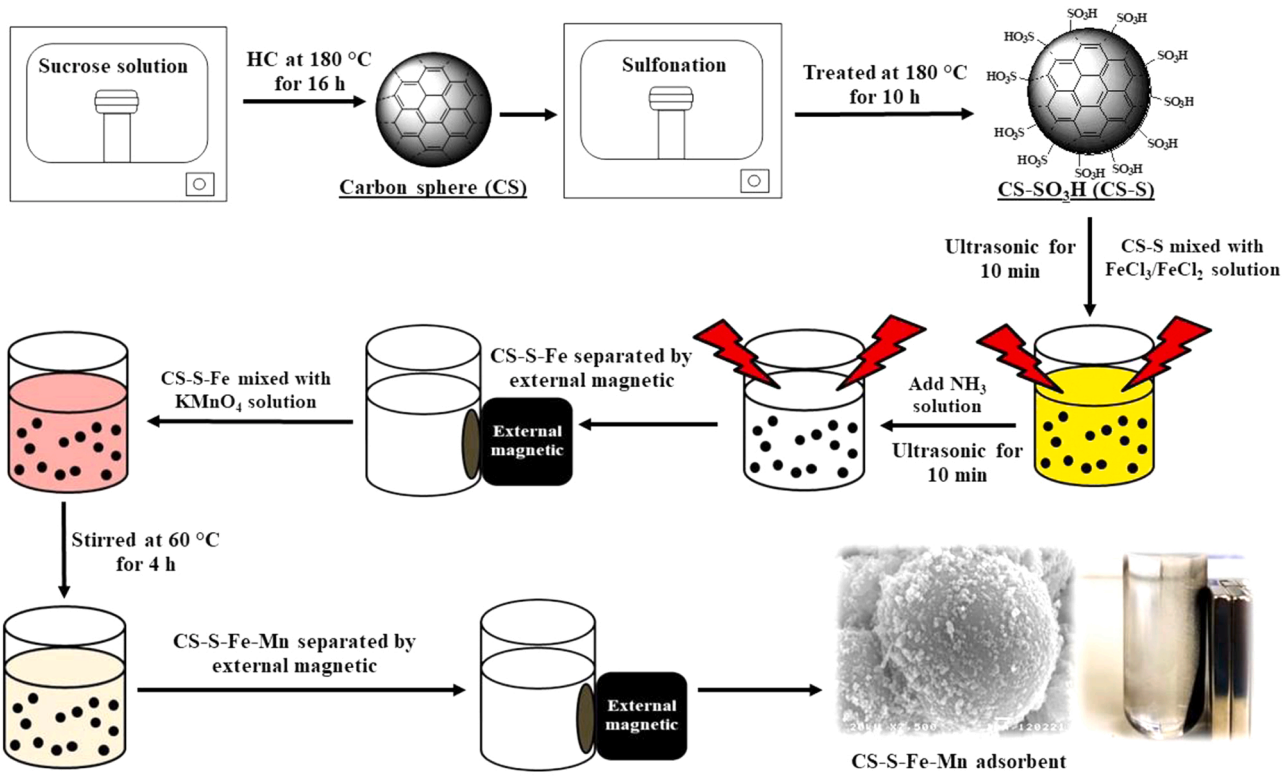

Fig. 1. Scheme illustration for preparation steps of magnetic CS-S-Fe-Mn adsorbent.

150 rpm. The pH conditions were adjusted by using hydrochloric or sodium hydroxide solution at a concentration of 0.1 mol/L. After finishing test, the adsorbent was recovered from aqueous solution using a neodymium magnet. For desorption process, the spent adsorbent was performed by soaking in nitric acid solution at a concentration of 1 mol/L [32]. The concentrations of Pb^{2+} remaining were analyzed by a Flame Atomic Absorption spectrometer (Thermo scientific iCE3000) using an external standard method. Various factors such as adsorbent type, pH values, initial concentration of Pb^{2+}, contact time, and temperature were investigated. The adsorption capacity at equilibrium condition (q_e, mg/g) was calculated using the following Eq. (1):

$$q_e = \frac{(C_0 - C_e)V}{M} \quad (1)$$

where C_0 and C_e are the initial and equilibrium concentration (mg/L) of adsorbate, respectively, V is the initial volume of the aqueous solution (L) and M is the amount of adsorbent (g).

Herein, total adsorption experiments were replicated at least three times to ensure the preciseness. The error bars derived from tSE in each experiment was calculated as the following Eq. (2):

$$\mathrm{tSE} = \frac{\mathrm{t} \times \mathrm{s}}{\sqrt{\mathrm{n}}} \quad (2)$$

where t is the student's test, s is the standard deviation and n is the number of observations.

The details of experimental conditions on adsorption isotherm/kinetic/thermodynamic are given in SI. For adsorption models, Langmuir, Freundlich, Temkin, Dubinin-Radushkevich, Redlich-Peterson and/or Toth isotherms were investigated at different concentrations of Pb^{2+} solution. Herein, the adsorption mechanisms such as monolayer and multilayer were identified by Langmuir and Freundlich isotherms, respectively [33,34]. The calculation and determination of Langmuir parameters are written as the following Eq. (3):

$$\mathrm{q_e} = \frac{\mathrm{q_{max}KC_e}}{1 + \mathrm{KC_e}} \quad (3)$$

where q_{max} is the maximum adsorption capacity (mg/g) and K is the Langmuir coefficient (L/mg).

The calculation and determination of Freundlich parameters are given by the following Eq. (4):

$$\mathrm{q_e} = K_F C_e^{1/n} \quad (4)$$

where K_F is the Freundlich coefficient and n is the heterogeneity parameter that represents the bonding spread.

Temkin isotherm was used to gauge the interaction between adsorbent and adsorbate [35]. The calculation and determination of Temkin parameter are given by the following Eq. (5):

$$\mathrm{q_e} = \left(\frac{\mathrm{RT}}{\mathrm{b}}\right)\ln(\mathrm{AC_e}) \quad (5)$$

Where R is the universal gas constant (8.314 J/molK^{-1}), A is this equilibrium constant correlated to highest binding energy (L/mol), T is the adsorption temperature (K) and b is the Temkin coefficient correlated to heating adsorption.

Dubinin-Radushkevich model was utilized to assign the relation between apparent free energy and adsorption behavior [36]. The calculation and determination of Dubinin-Radushkevich parameter are provided by the following Eq. (6):

$$q_e = q_s \exp\left(-B\varepsilon^2\right) \quad (6)$$

where q_s is the theoretic saturation capability (mg/g), B is the Dubinin-Radushkevich coefficient correlated to biosorption energy (mol^2/kJ) and Ɛ is Polanyi potential adsorption.

Meantime, adsorption free energy (E, kJ/mol) was determined by the following Eq. (7):

$$E = \frac{1}{\sqrt{2B}} \tag{7}$$

Redlich-Peterson isotherm is written by the following Eq. (8):

$$q_e = \frac{AC_e}{1 + BC_e^g} \tag{8}$$

Where A, B and g is the constant value by $0 < g < 1$. (g =1, Langmuir isotherm).

Toth model was proposed to apply for heterogeneous adsorption proved from potential theory by assuming to Quasi-Gaussian energy, which surface of adsorption energy had lower than maximum energy value of adsorption. The calculation and determination of Toth parameter are written as the following Eq. (9):

$$q_e = \frac{q_e^{\infty} C_e}{\left[K_{Th} + C_e^{Th}\right]^{1/Th}} \tag{9}$$

where q_e^{∞} is equilibrium capability based on monolayer adsorption (mg/g), K_{Th} is the Toth coefficient.

The adsorption kinetic was simulated to find the adsorption rate utilizing pseudo first-order and pseudo second-order kinetic model. The kinetic parameters are determined by nonlinear regression in excel using Eqs. (10) and (11), respectively [37]:

$$q_t = q_e\left(1 - e^{-k_1 t}\right) \tag{10}$$

$$q_t = \frac{q_e^2 k_2 t}{1 + q_e k_2 t} \tag{11}$$

where q_t is the equilibrium capability (mg/g) at any adsorption time. t is

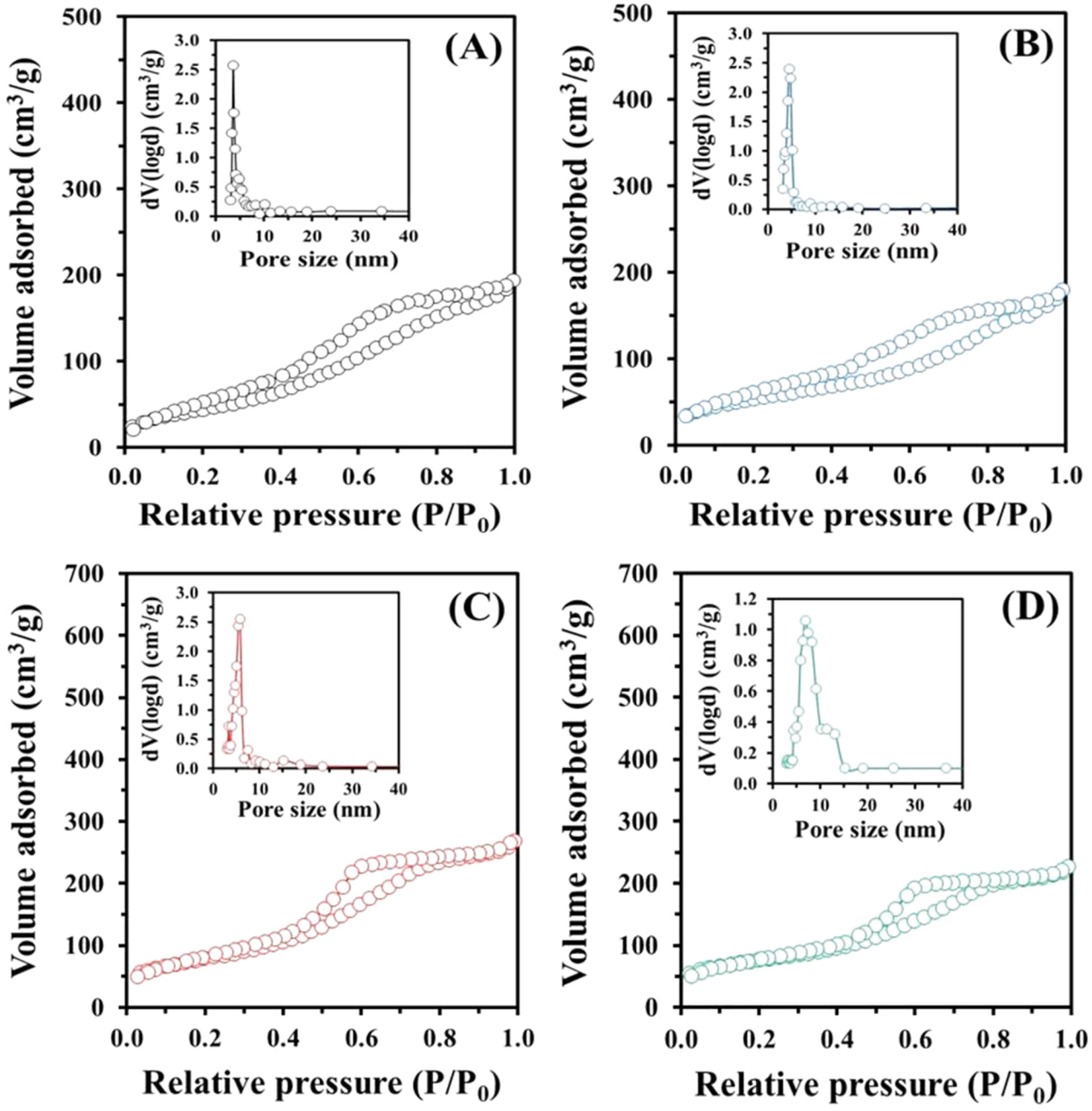

Fig. 2. N_2 sorption isotherms and pore size distributions of (A) CS, (B) CS-S, (C) CS-S-Fe and (D) CS-S-Fe-Mn.

the adsorption time (min). k_1 and k_2 are the pseudo first-order and pseudo second-order rate constants, respectively.

Intra-particle diffusion over Weber-Morris model was used to determine for Pb^{2+} adsorption step. The calculation and determination of Weber-Morris parameter are provided as the following Eq. (12):

$$q_t = k_p t^{1/2} \quad (12)$$

where k_p is the rate constant of Pb^{2+} diffusion on adsorbent structure.

Each factor of thermodynamic adsorption such as Gibbs free energy (ΔG, kJ/mol), standard enthalpy (ΔH, kJ/mol) and standard entropy (ΔS, J/mol·K) are calculated using the following Eqs. (13)–(15) [38]:

$$K_d = \frac{C_o - C_e}{C_e} \quad (13)$$

$$\Delta G = -RT \ln K_d \quad (14)$$

$$\ln K_d = \frac{\Delta S}{R} - \frac{\Delta H}{RT} \quad (15)$$

where K_d is the is the thermodynamic equilibrium coefficient and T is the adsorption temperature (K).

3. Results and discussion

3.1. Physical and chemical properties of each adsorbent

Fig. 2 shows the N_2 adsorption-desorption isotherms and pore size distributions of CS, CS-S, CS-S-Fe and CS-S-Fe-Mn. As obtained, the isotherms of all adsorbents exhibited the hysteresis loop type H2 isotherm with narrow pore size distribution around 3–10 nm, corresponding to complex mesoporous material with percolation in pore necks [38,39]. Meanwhile, their volumes of hysteresis loop for N_2 adsorption were increased to some extent, resulting from surface modification by Fe_3O_4 and MnO_2. The textual properties of virous adsorbents were also supported, and the results are shown in Table 1. One can see that the CS-S after hydrothermal sulfonation process had a lowest surface area with pore volume, suggesting that sulfonic groups were well distributed and covered on CS surface. Interestingly, after modification by Fe_3O_4 and MnO_2, the CS surface area was clearly increased up to ~1.7 times, indicating that new unique-rudeness surface area with larger pore volume on CS structure were regenerated. This phenomenon should be a reason for improving the removal efficiency of Pb^{2+} since more available of active sites were existed.

Fig. 3 shows the XRD patterns of various magnetic adsorbents. The XRD diffraction peaks at 30, 35, 43, 54, 57 and 63° were assigned to the planes of (220), (311), (400), (422), (511) and (440), corresponding to Fe_3O_4 crystal or magnetic structure [40]. Each reaction step for Fe_3O_4 formation is given as the following Eqs. (16)–(19) [41]:

$$Fe^{3+} + 3OH^- \rightleftharpoons Fe(OH)_3 \quad (16)$$

$$Fe(OH)_3 \rightleftharpoons FeOOH + H_2O \quad (17)$$

$$Fe^{2+} + 2OH^- \rightleftharpoons Fe(OH)_2 \quad (18)$$

$$2FeOOH + Fe(OH)_2 \rightleftharpoons Fe_3O_4 + 2H_2O \quad (19)$$

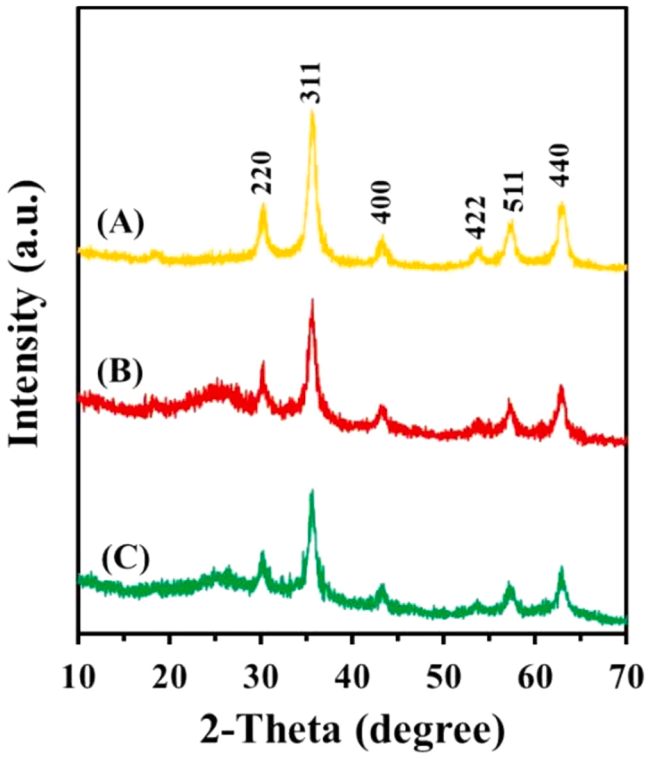

Fig. 3. XRD patterns of (A) pure Fe_3O_4, (B) CS-S-Fe and (C) CS-S-Fe-Mn.

The broad peaks at a range of 20–30° for CS-S-Fe and CS-S-Fe-Mn was accorded to carbon structure [42]. It should be noted that the diffraction peaks of MnO_2 did not observe in CS-S-Fe-Mn since the similar patterns around 30, 36 and 43° was interposed with Fe_3O_4 structure [43]. As can be seen, the intensity of Fe_3O_4 diffraction peak in CS-S-Fe-Mn was lower than CP-Fe-Mn, resulting from the well coating by MnO_2 particles.

Fig. 4 shows the presence of functional groups on each adsorbent by FT-IR spectra results. One can see that oxygen containing functional groups such as -C-O/O═S═O, -SO_3H, -C═O and -OH were obviously appeared for all absorbents at wavenumbers of 1032, 1171, 1630 and 3400 cm^{-1}, respectively [44]. The strong vibration peak at wavenumber of 560 cm^{-1} was found in CS-S-Fe and CS-S-Fe-Mn which should be described for Fe–O functional group of Fe_3O_4 [45]. The MnO_2 functional group for CS-S-Mn was detected at ~500 cm^{-1} which was quite near to Fe_3O_4 diffraction peak. The magnetization hysteresis loops and VSM results of CS-S-Fe and CS-S-Fe-Mn are shown in Fig. 5A, B and Table S1. As observed, the narrow hysteresis loops under the ranges of applied fields around −12,000–12000 Oe were observed for both adsorbents. The saturation magnetization values of CS-S-Fe and CS-S-Fe-Mn were 21.8 and 20.9 emu/g, respectively, suggesting the paramagnetic features in nature [46]. The lower saturation magnetization values of CS-S-Fe-Mn should be due to the addition of non-magnetic MnO_2 on adsorbent surface. However, this was still enough to be simply separated from solution system for ~30 s using an exterior magnetic field (Fig. 5C).

Table 1
Physical and chemical properties of various adsorbents.

Adsorbent	Surface area (m^2/g)	Pore volume (cm^3/g)	Amount of functional group (mmol/g)				
			Carboxylic	Lactone	Phenolic	Total acidity	Total basicity
CS	89	0.89	0.0256	0.0233	4.2156	4.2645	0.0566
CS-S	85	0.81	1.2115	1.2223	2.2212	4.6550	0.0416
CS-S-Fe	153	1.07	0.6400	0.6202	1.1215	2.3817	2.1561
CS-S-Fe-Mn	146	0.96	1.2458	1.2355	0.8256	3.3069	4.5644

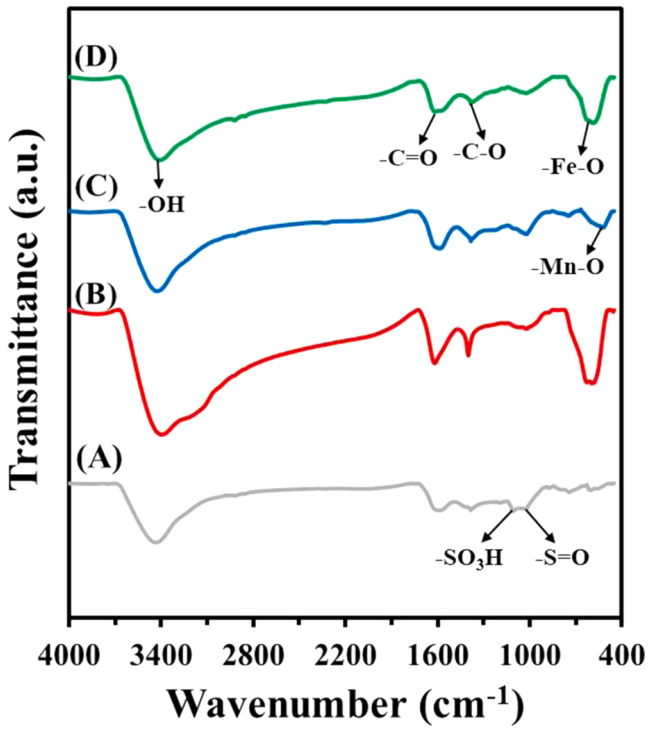

Fig. 4. FT-IR spectra of (A) CS-S, (B) CS-S-Fe, (C) CS-S-Mn and (D) CS-S-Fe-Mn.

The morphologies and the distribution of element species on CS, CS-S, CS-S-Fe and CS-S-Fe-Mn were observed by SEM-EDS images, and their results are shown in Fig. 6. As expected, CS morphology presented the spherical shape with smooth surface nature which generally occurred via hydrothermal carbonization of sugar. After sulfonation, characteristic of morphological structure of CS did not change but there were some flake particles on CS-S surface. Interestingly, when Fe_3O_4 and MnO_2 were coated on CS-S surface, rough surfaces (petal-like walls) were observed in CS-S-Fe and CS-S-Fe-Mn. For pure MnO_2, uniform rod-like nanoparticles with smooth surface were obtained via hydrothermal precipitation process (Fig. S5). The amounts of various elements such as C, O, S, Fe and Mn on CS-S, CS-S-Fe and CS-S-Fe-Mn are given in Table S2. As also shown in Fig. 6, the EDS mapping images of each adsorbent demonstrate that S, Fe and Mn elements were well dispersed on the adsorbent surfaces without accumulation pattern.

The surface charge properties of CS-S-Fe-Mn were defined from pH_{pzc} technique, and the results are shown in Fig. 7 and Table S3. As shown in Fig. 7, before addition of CS-S-Fe-Mn, the detected pH was normally increased based on adjustment of initial pH from 2 to 10. However, at an initial pH of 2, the pH value detected in mixture solution after addition of CS-S-Fe-Mn was clearly increased, suggesting that proton in solution was significantly reduced, resulting from mutual interaction with CS-S-Fe-Mn surface. This confirms that basicity and negative charge properties of CS-S-Fe-Mn were quite remarkable. In addition, the pH value detected in mixture solution after addition of CS-S-Fe-Mn were > 7 with the increasing of initial pH from 3 to 10. As can be seen at an intersection point, the point of zero charge (pzc) in this system was at about 8.6. As also shown in Table S3, it is found that pH_{pzc} value of CS-S-Fe-Mn was higher than pH of mixture solution (CS-S-Fe-Mn + Pb^{2+} ion), indicating that surface properties of CS-S-Fe-Mn were entirely possessed by negative charge at $pH < pH_{pzc}$, resulting in well performance for Pb^{2+} removal process. The acidic-basic properties of CS, CS-S, CS-S-Fe and CS-S-Fe-Mn are presented in Table 1. One can see that CS had lower carboxylic and lactone groups than CS-S. However, the hydrothermal carbonization/sulfonation processes resulted in significant reduction of phenolic group on CS-S. After Fe_3O_4 coating on CS-S surface, its acidic properties were decreased to some extent while basicity was increased

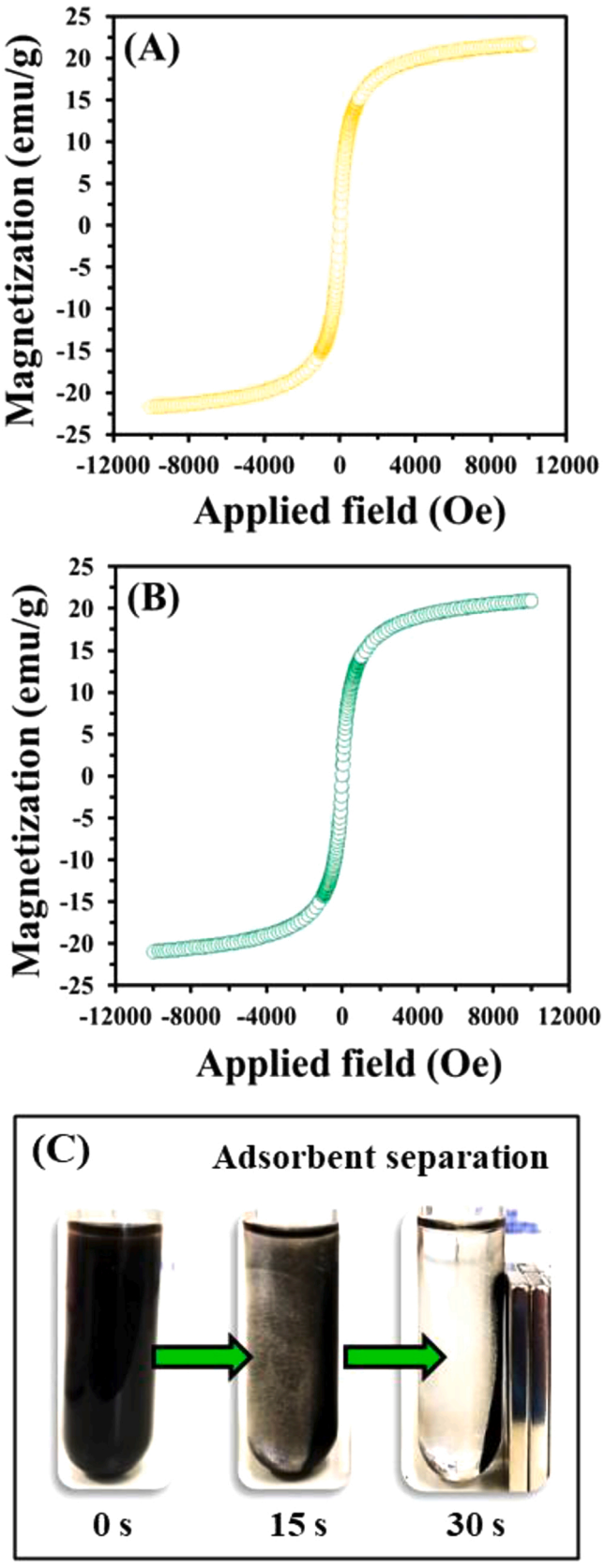

Fig. 5. Magnetization curves of (A) CS-S-Fe and (B) CS-S-Fe-Mn. (C) Dispersion appearance of adsorbent particle and separation process by external magnetic field.

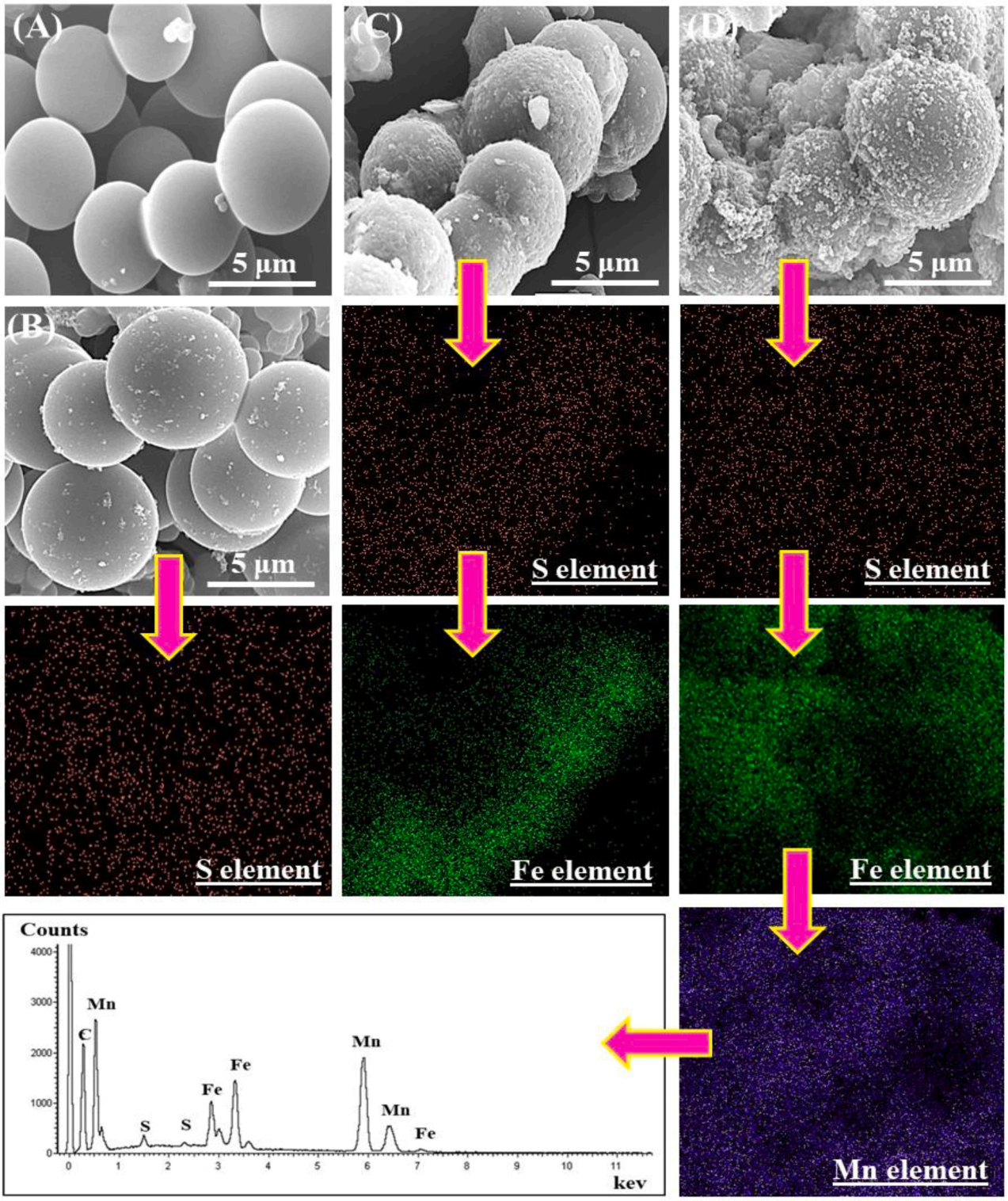

Fig. 6. SEM-EDS images of (A) CS, (B) CS-S, (C) CS-S-Fe and (D) CS-S-Fe-Mn.

from 0.04 to 2.16 mmol/g. However, the carboxylic and lactone groups as well as acidity were anew increased when CS-S-Fe was doped by MnO_2. This indicates that hydroxyl group (-OH) could easily oxidized and converted to carboxylic groups (-COOH) via $KMnO_4$ modification process [47]. A highest basicity of 4.56 mmol/g was found in CS-S-Fe-Mn which might be a reason improving the adsorption capacity of Pb^{2+}. The existence of Fe_3O_4 and MnO_2 on CS-S adsorbent could react with HCl during titration process, leading to higher basic properties.

3.2. Adsorbent behaviors of Pb^{2+} onto each adsorbent

The roles of Pb^{2+} adsorption onto various adsorbents such as CS, CS-S, CS-Mn, CS-S-Mn, CS-S-Fe, CS-S-Fe-Mn, CS-Mn-S and pure MnO_2 are presented in Fig. 8. Herein, the adsorption capacity at equilibrium condition (q_e value) was applied as an indicator for identifying the adsorption efficiency in each adsorbent. As observed, the CS-S-Fe-Mn exhibited a highest capacity of Pb^{2+} adsorption (137.11 mg/g) while a

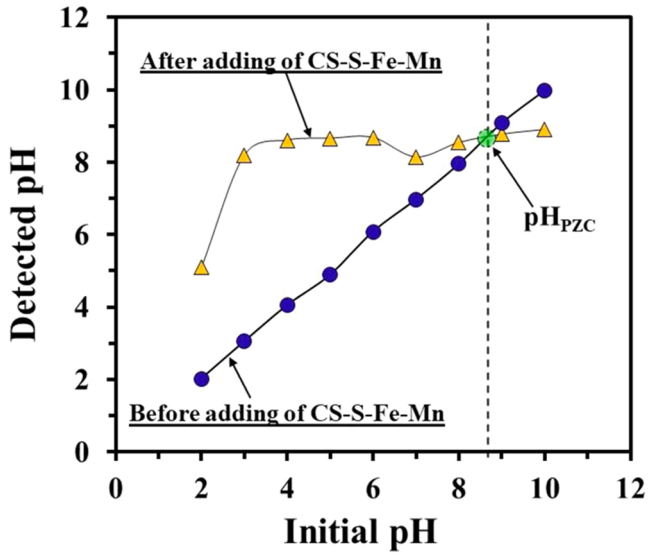

Fig. 7. pH_{pzc} curves of CS-S-Fe-Mn.

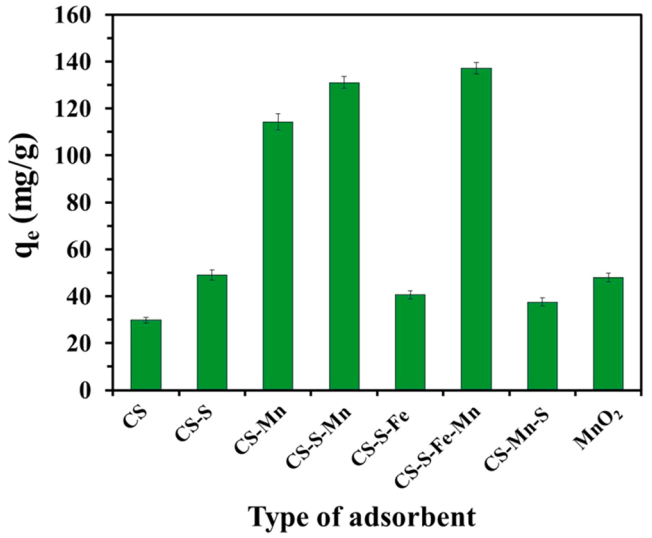

Fig. 8. Adsorption capacities of Pb^{2+} onto various adsorbents. The initial concentration of adsorbate (C_0) of Pb^{2+} = 600 mg/L, adsorbate volume = 25 mL, adsorbent amount = 0.1 g, time (t) = 30 min and temperature (T) = 303 K.

lowest capacity of 29.86 mg/g was found in CS without any modification. This indicates that the contribution of oxygen atoms derived from SO_3H-, Fe_3O_4 and MnO_2 on CS surface had great effect for improving the Pb^{2+} adsorption performance. Remarkably, the adsorption efficiency of Pb^{2+} was increased up to two times after CS was sulfonated (CS-S, q_e = 49.04 mg/g), comparing with CS without modification. When CS and CS-S were modified by $KMnO_4$, higher adsorption efficiencies of Pb^{2+} were significantly obtained. The removal efficiency of CS-S-Fe (q_e = 40.67 mg/g) had much lower than that of CS-S-Mn (q_e = 114.33 mg/g), suggesting that the presence of MnO_2 on adsorbent support was highly desired for efficient removal of Pb^{2+} ion. It also discloses that Fe_3O_4 nanoparticles enveloped on CS-S surface were highly benefit for recovery process but only slight improvement for adsorption efficiency of Pb^{2+} was obviously identified. The removal efficiency was extremely reduced up to ~60% when CS-Mn-S (qe = 37.53 mg/g) was utilized to replace the CS-S-Mn, indicating that the order of modification process should be considered by hydrothermal sulfonation at first and then followed by oxidation process. The adsorption capacities of Pb^{2+} were in the sequence of CS-S-Fe-Mn>CS-S-Mn>CS-Mn>CS-S> pure MnO_2>CS-S-Fe >CS-Mn-S>CS. The better adsorption efficiency of Pb^{2+} ion from aqueous solution over CS-S-Fe-Mn could be described by the abundant existence of oxygen containing functional groups such as sulfonic/carbonyl/carboxylic groups/MnO_2 on CS surface newly created via hydrothermal sulfonation and $KMnO_4$ modification as the following Eqs. (20) and (21) [48]:

$$–C–C–C– + –C–C–C–OH + H_2SO_4 \rightarrow – C–C{=}O + –C–COOH/–C–SO_3H \quad (20)$$

$$–C–C–C–OH + KMnO_4 \rightarrow –C–COOH + –C–C{=}O + MnO_2 \quad (21)$$

In this case, Pb^{2+} ion (Lewis acid properties) could be easily adsorbed onto CS-S-Fe-Mn surface containing abundant amount of oxygen functional groups (Lewis base properties) such mentioned above through co-attraction between electrostatic force with co-ordinate covalent bond [49]. In the other words, the existence of active sites and lone pair electrons was answerable for sufficient interaction with proton metal ions. As known that lone pairs electrons could create the coordination/complexation bonds with Pb^{2+} during the adsorption procedure. Also, the synergetic effect between MnO_2 with sulfonated carbon surface as well as increasing of surface area (more available active sites/surface functional groups) might be the reasons for great improving the Pb^{2+} adsorption efficiency/accessibility. It should be mentioned here that the coating by only Fe_3O_4 resulted in the slight increasing of adsorption efficiency due to its stability in form of ionic state, while the existences of MnO_2, C=O, -COOH and/or -SO_3H were much better. Since they had covalent bonds, the lone pair of electrons could be endowed to create the attraction force with the Pb^{2+} via sharing the electron pair [50]. As mentioned, these adsorption mechanisms of Pb^{2+} were also well supported by spectroscopic evidence from previous study [51]. To reach more details on adsorption behaviors, isotherm/kinetic/thermodynamic models were investigated and discussed in the Section 3.4. Fig. 9 shows the adsorption ability of Pb^{2+}, Cr^{6+}, Fe^{2+}, Cd^{2+} and Hg^{2+} onto CS-S-Fe-Mn. The adsorption selectivity was increased following the sequence of $Pb^{2+} > Fe^{2+} > Cr^{6+} > Cd^{2+} > Hg^{2+}$. The highest and lowest capacities were found in adsorptions of Pb^{2+} (137.11 mg/g) and Hg^{2+} (13.56 mg/g), respectively. It is possible that Pb^{2+} had softer feature than other metal ions which highly favored over CS-S-Fe-Mn adsorbent, resulting in better selectivity for adsorption process [46,52]. Based on these results, CS-S-Fe-Mn was selected as a best adsorbent for further studies including adsorption selectivity, pH

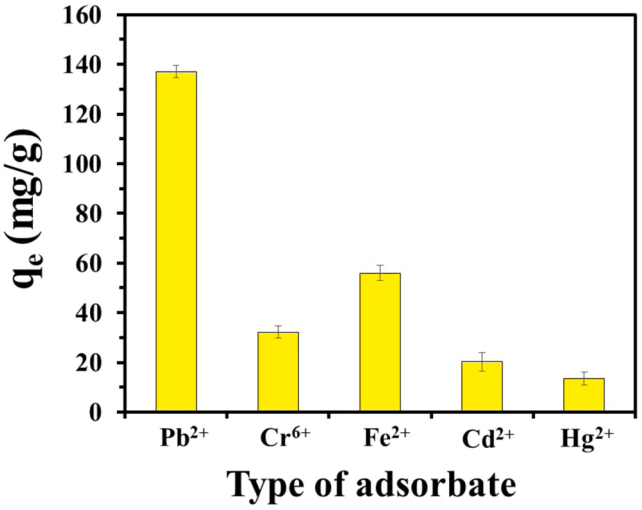

Fig. 9. Adsorption capacities of each metal ion onto CS-S-Fe-Mn. The initial concentration of adsorbate (C_0) = 600 mg/L, adsorbate volume = 25 mL, adsorbent amount = 0.1 g, time (t) = 30 min and temperature (T) = 303 K.

values, initial concentration of Pb^{2+}, adsorption time and temperature.

3.3. Role of pH for Pb^{2+} adsorption

The pH value is an essential parameter for investigating the adsorption performance of CS-S-Fe-Mn which also resulted in the surface charge properties of the adsorbent and the presence of lead form in aqueous solution. Therefore, the role of pH value (1−9) in solution for Pb^{2+} adsorption onto CS-S-Fe-Mn, the results are shown in Fig. 10. One can see that the adsorption ability of Pb^{2+} was increased to some extent with the increase of pH value in solution. As known that higher amount of hydronium ion was generally found at lower pH value, leading to facile perturbation of adsorption ability. In this case, the abundant occurrence of hydronium ion could interact with MnO_2 on adsorbent, resulting in a positive charge on active site of adsorbent, leading to low performance of Pb^{2+} adsorption [53]. Also, the magnetic properties of CS-S-Fe-Mn were easily destroyed at low pH condition which affected to difficult separation process. In addition, at the pH value of > 7, Pb^{2+} ions could be existed in precipitation form of $Pb(OH)_2$ [54]. From these results, all adsorption experiments were performed at pH value of 7, which could be considered as a suitable condition for application in environmentally treatment process. The result of Pb^{2+} desorption from spent CS-S-Fe-Mn is shown in Fig. S6. Firstly, spent CS-S-Fe-Mn after Pb^{2+} adsorption process was washed with distilled water to eliminate the unabsorbed ions, and then desorbed by soaking in nitric acid solution at a concentration of 1 mol/L. It is found that the ability of Pb^{2+} desorption could be achieved by washing with nitric acid solution [47]. However, the desorption process should be also affected with Fe_3O_4 and MnO_2 coated on CS-S surface since CS-S-Fe-Mn surface was protonated, leading to desorption of other metal cations such as Fe^{2+} and Mn^{2+}, resulting in poor reusability. Thus, it may be further considered for regeneration process via simple precipitation methods before reusability test.

3.4. Isotherm/kinetic/thermodynamic of Pb^{2+} adsorption onto CS-S-Fe-Mn

Fig. 11 and Table 2 present the adsorption behaviors/parameter of Pb^{2+} onto CS-S-Fe-Mn through various model isotherms. The data were defined using non-linear method. Considering between Langmuir with Freundlich isotherm, the adsorption consequences had more proper with the Langmuir isotherm ($R^2 = 1.0000$) than that of the Freundlich isotherm ($R^2 = 0.9246$). This indicates that monolayer adsorptions of

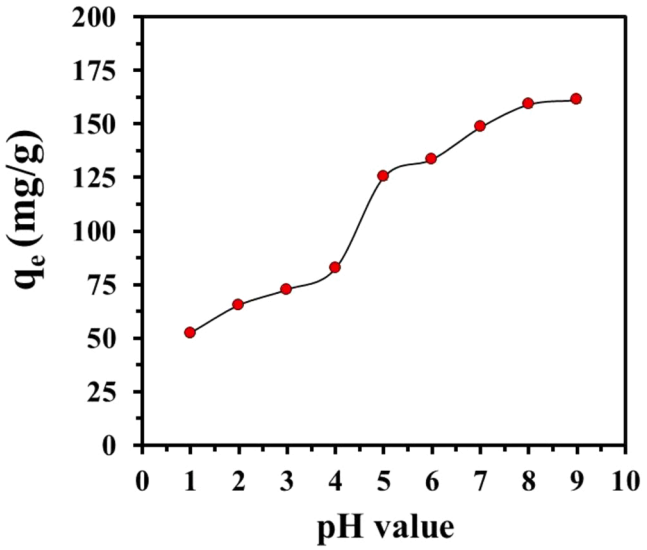

Fig. 10. Role of pH value on the adsorption ability of Pb^{2+} onto CS-S-Fe-Mn.

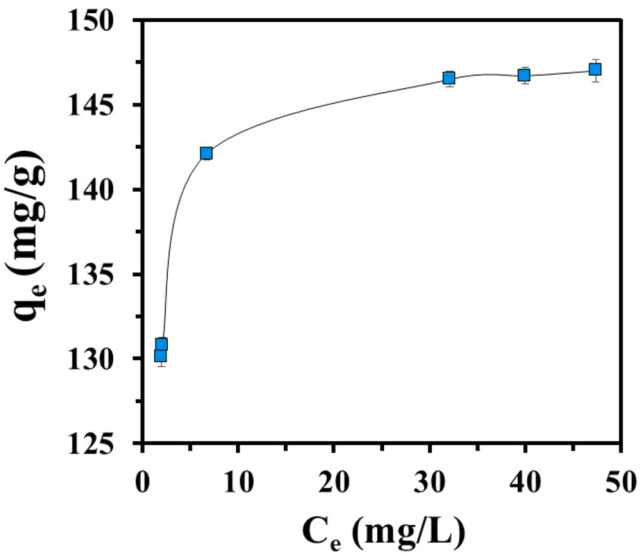

Fig. 11. Adsorption behavior of Pb^{2+} onto CS-S-Fe-Mn at equilibrium conditions. The initial concentration of adsorbate (C_0) of Pb^{2+} = 500–800 mg/L, adsorbate volume = 25 mL, adsorbent amount = 0.1 g, time (t) = 30 min and temperature (T) = 303 K.

Pb^{2+} (Lewis acid/positive charge) were performed on CS-S-Fe-Mn surface (in the presence of Lewis base and/or lone pair electrons obtained from each functional group along with negative surface charge at $pH_{pzc} > 7$) through electrostatic mechanism with the assistant of co-ordinate covalent bond. A maximum adsorption capacity (q_{max}) of Pb^{2+} onto CS-S-Fe-Mn could reach to 147.76 mg/g based on Langmuir model, which were acceptable after comparison with other magnetic adsorbents in the previous literatures (Table 3) [11,28,46,55–65]. As such, an excellent adsorption efficiency of Pb^{2+} over CP-S-Fe-Mn low-cost magnetic adsorbent might mainly benefit from the synergistic effect of oxygen functional groups such as -C═O, C-O and -SO_3H as well as MnO_2. However, the main problem of CP-S-Fe-Mn was an instability when desorption process was applied, which further required for regeneration process. For Temkin isotherm, the R^2 value of Pb^{2+} adsorption process was closed to 1 ($R^2 = 0.9978$), indicating that Pb^{2+} could be strongly anchored on CS-S-Fe-Mn surface with a *A* value of 2.57×10^{13} L/mol. In the case of Dubinin-Radushkevich isotherm, it should be regarded since R^2 value was 0.9823 for Pb^{2+} adsorption behavior. Herein, E value of Pb^{2+} adsorption onto CS-S-Fe-Mn was lower than 8 kJ/mol, resulting from electrostatic interaction via physisorption mechanism [66]. Remarkably, q_s value derived from Dubinin-Radushkevich model was also close to q_{max} value of Langmuir model, supporting the more accuracy on isotherm model. The parameters derived from Toth and/or Redlich-Peterson were applied to ensure on assumption of Langmuir isotherm. As expected, g constant, Th and their R^2 values derived from both models were almost equal to 1. This could be concluded that adsorption mechanism of Pb^{2+} onto CS-S-Fe-Mn was monolayer pattern.

Fig. 12A shows the adsorption efficiency of Pb^{2+} onto CS-S-Fe-Mn at different contact times of 3–70 min. Herein, a fast rate of Pb^{2+} adsorption was initially observed at contact time of 3 min, resulting from the sufficient available of adsorption sites on CS-S-Fe-Mn. Then, the removal efficiency of Pb^{2+} was slowly increased with an increase in contact time until adsorption equilibrium was reached at 30 min. The Pb^{2+} ion diffusion became tardy when active sites on CS-S-Fe-Mn surface was occupied by Pb^{2+} ion. To get more details on adsorption kinetic rate, as shown in Table 2, the kinetic model with a pseudo second-order for Pb^{2+} adsorption onto CS-S-Fe-Mn presented a R^2 value of 1.0000 while pseudo first-order model did not approach to 1, resulting from a fast adsorption rate occurred between Pb^{2+} ions with CS-S-Fe-Mn. Moreover, the $q_{e\ cal}$ data (147.63 mg/g) derived from second-order kinetic

Table 2
Isotherm, kinetic and thermodynamic parameters and their correlation coefficients for selective adsorption of Pb^{2+} onto CS-S-Fe-Mn.

Adsorption equilibrium							
Langmuir parameters				Freundlich parameters			
q_{max}/(mg/g)		K (L/mg)	R^2	1/n	K_F	R^2	
147.76		3.72	1.0000	0.0373	128.40	0.9246	
Temkin parameters				Dubinin-Radushkevich parameters			
b		A (L/mol)	R^2	q_s/(mg/g)	B/(mol^2/kJ)	*E*/(kJ/mol)	R^2
588.74		2.57×10^{13}	0.9978	146.19	1.16×10^{-7}	2.93	0.9823
Redlich-Peterson parameters				Toth parameters			
A	B	g	R^2	q_e^{∞}	K_{Th}	Th	R^2
547.84	3.71	1.00	1.0000	147.73	0.272	1.01	1.0000
Adsorption kinetic							
$q_{e\ exp}$ (mg/g)	Pseudo-first-order			Pseudo-second-order			
	$q_{e\ cal}$	k_1	R^2	$q_{e\ cal}$	k_2	R^2	
147.30	6.151	0.075	0.9284	147.63	0.038	1.0000	
Adsorption thermodynamic							
ΔS (J/molK)	ΔH (kJ/mol)	ΔG (kJ/mol)				R^2	
		303 K	313 K	323 K	328 K		
190.28	49.12	-8.43	-9.81	-11.16	-12.18	0.9917	

Table 3
Comparison of adsorption abilities of Pb^{2+} by different magnetic adsorbents.

Adsorbent	q_{max} of Pb^{2+} (mg/g)	Ref.
Mt@MH	38.15	[11]
CP-Fe-Mn	49.64	[28]
L1@MNP	111.23	[46]
MBC	25.29	[55]
MBC	26.08	[56]
MECBC	40.57	[57]
MCW-2	41.19	[58]
Fe_3O_4-GS	27.95	[59]
M-Lignin-PEI	96.60	[60]
LDMHMs	33.00	[61]
Magnetic-biochar	64.13	[62]
Fe_3O_4-SO_3H MNPs	108.93	[63]
Fe_3O_4@SiO_2-PEI-SH	110.13	[64]
Fe_3O_4-CS-L	128.63	[65]
CS-S-Fe-Mn	147.76	This work

was good consistent with the experimental data (147.30 mg/g), indicating that this kinetic model had high preciseness. Fig. 12B shows the plots of intra-particle diffusion for adsorption of Pb^{2+} onto CS-S-Fe-Mn over Weber-Morris model. The multi-linearity pattern was observed, suggesting that intra-particle diffusion along with diffusion steps were occurred from Pb^{2+} adsorption mechanism [67,68]. The adsorption mechanism of Pb^{2+} onto CS-S-Fe-Mn could be described via diffusion two steps of confines layer as follows: the abrupt adsorption at exterior surface of CS-S-Fe-Mn was started in the first step, and then the final adsorption phase was activated at low concentration amount of Pb^{2+} over intra-particle diffusion at retarding process.

The thermodynamic adsorption process of Pb^{2+} onto CS-S-Fe-Mn was carried out at different temperatures of 303, 313, 323 and 328 K. As presented in Fig. 13, a multiplication of Pb^{2+} adsorption temperature could augment the removal efficiency of Pb^{2+} onto CS-S-Fe-Mn, indicating to nature of endothermic adsorption. Furthermore, better diffusion rate of Pb^{2+} was also supported via diffusion at internal pore and the external boundary layer of the CS-S-Fe-Mn structure along with significant reduction of viscosity in the solution system. As presented in Table 2, the negative values of ΔG at temperatures of 303–328 K derived from selective adsorption of Pb^{2+} onto CS-S-Fe-Mn were found in the range between −12.18 and −8.43 kJ/mol. Herein, the spontaneous nature was observed when the negative values of ΔG was incessantly reduced with an increase in adsorption temperature [69]. As known that the ΔG ranges of physisorption and chemisorption behaviors were −20–0 and −80 to −400 kJ/mol, respectively. This ensures that adsorption behavior of Pb^{2+} onto CS-S-Fe-Mn was physisorption process. Moreover, the positive value of 49.12 kJ/mol was obtained for ΔH

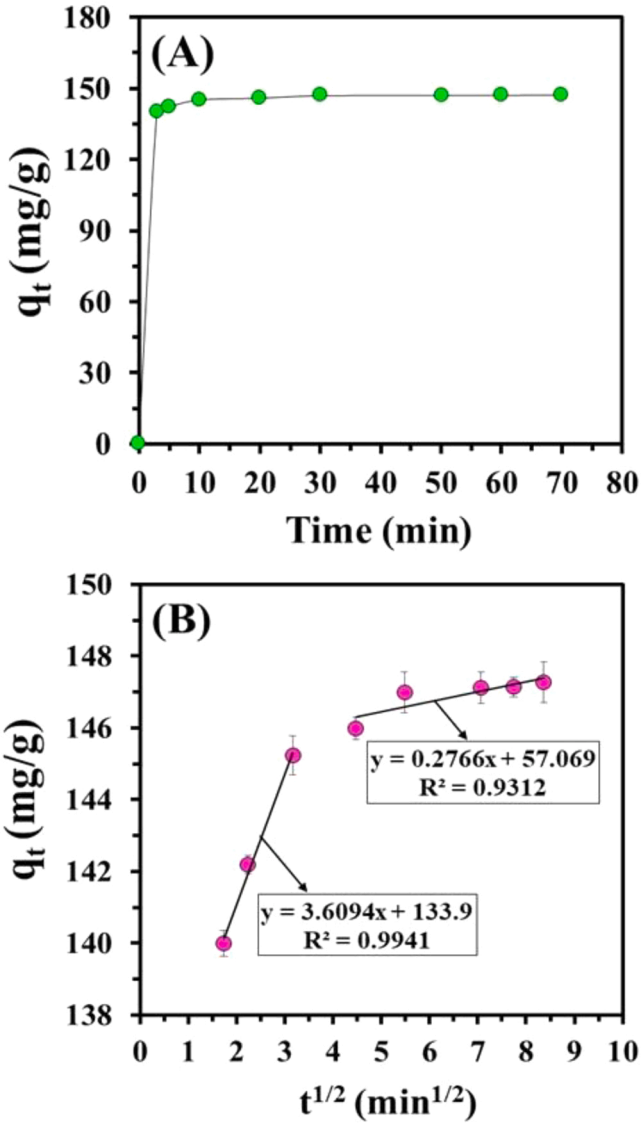

Fig. 12. Roles of (A) contact time and (B) intra-particle diffusion plots for selective adsorption of Pb^{2+} onto CS-S-Fe-Mn. The initial concentration of adsorbate (C_0) of Pb^{2+} = 600 mg/L, adsorbate volume = 25 mL, adsorbent amount = 0.1 g, time (t) = 3–70 min and temperature (T) = 303 K.

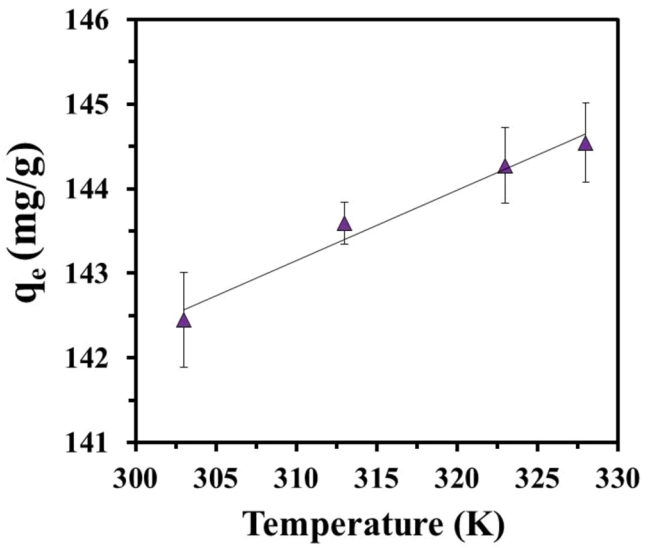

Fig. 13. Role of temperature for selective adsorption of Pb^{2+} onto CS-S-Fe-Mn. The initial concentration of adsorbate (C_0) of Pb^{2+} = 600 mg/L, adsorbate volume = 25 mL, adsorbent amount = 0.1 g, time (t) = 30 min and temperature (T) = 303–328 K.

value, indicating that Pb^{2+} adsorption process over CS-S-Fe-Mn were under spontaneous endothermic reaction [70]. In this case, physisorption process was also supported since ΔH value was lower 100 kJ/mol, which was in good conformity versus Dubinin-Radushkevich model. In addition, an increase of haphazardness between CS-S-Fe-Mn interface with Pb^{2+} ion was initiated at a positive value of ΔS (190.28 J/molK) under the adsorption process.

4. Conclusions

The facile preparation of magnetic CS-S-Fe-Mn adsorbent was successfully achieved via hydrothermal carbonization/sulfonation and followed by facile precipitation processes. After modification process, higher surface area, larger pore volume and higher basicity were found together with the abundant existences of oxygen functional groups such as -C-O/C═O, -COOH and -SO_3H as well as MnO_2, leading to excellent enhancement of Pb^{2+} adsorption capacity. For comparison using different adsorbents, CS-S-Fe-Mn presented the best performance for Pb^{2+} removal from aqueous solution. A suitable condition for Pb^{2+} removal in this study was fixed as follows: initial concentration of Pb^{2+} = 600 mg/L, initial volume of Pb^{2+} solution = 25 mL, CS-S-Fe-Mn amount = 0.1 g, adsorption time = 30 min and adsorption temperature = 303 K. A q_{max} value of Pb^{2+} adsorption onto CS-S-Fe-Mn was 147.76 mg/g which was higher performance than previous references. Furthermore, adsorption mechanisms of Pb^{2+} onto CS-S-Fe-Mn were corresponded to rapid monolayer-physisorption/spontaneous-endothermic natures. This research presented the co-integration process between potential removal of Pb^{2+} and facile recovery of adsorbent from water system. We expected that low-cost/green CS-S-Fe-Mn magnetic adsorbent might be further applied in practical treatment/purification of environmental wastewater.

CRediT authorship contribution statement

Panya Maneechakr: Supervision, Conceptualization, Project administration, Investigation Formal analysis, Validation. **Surachai Karnjanakom:** Methodology, Formal analysis, Writing – original draft, Writing - review & editing.

Declaration of Competing Interest

The authors declare that they have no known competing financial interests or personal relationships that could have appeared to influence the work reported in this paper.

Acknowledgements

The authors greatly acknowledge support from Department of Chemistry, Faculty of Science, Rangsit University for supporting all chemicals and apparatus. We also would like to gratefully appreciate the high valuable suggestions from all reviewers for improving the quality of this research.

Appendix A. Supporting information

Supplementary data associated with this article can be found in the online version at doi:10.1016/j.jece.2021.106191.

References

[1] I.V. Joseph, L. Tosheva, A.M. Doyle, Simultaneous removal of Cd(II), Co(II), Cu(II), Pb(II), and Zn(II) ions from aqueous solutions via adsorption on FAU-type zeolites prepared from coal fly ash, J. Environ. Chem. Eng. 8 (2020), 103895.
[2] R. Ahmad, A. Mirza, Adsorption of Pb(II) and Cu(II) by Alginate-Au-Mica bionanocomposite: kinetic, isotherm and thermodynamic studies, Process Saf. Environ. Prot. 109 (2017) 1–10.
[3] H.T.M. Thanh, T.T.T. Phuong, P.T.L. Hang, T.T.T. Toan, T.N. Tuyen, T.X. Mau, D. Q. Khieu, Comparative study of Pb(II) adsorption onto MIL–101 and Fe–MIL–101 from aqueous solutions, J. Environ. Chem. Eng. 6 (2018) 4093–4102.
[4] T. Şahan, Application of RSM for Pb(II) and Cu(II) adsorption by bentonite enriched with SH groups and a binary system study, J. Water Process Eng. 31 (2019), 100867.
[5] M. Naushad, T. Ahamad, K. Al-sheetan, Development of a polymeric nanocomposite as a high performance adsorbent for Pb(II) removal from water medium: equilibrium, kinetic and antimicrobial activity, J. Hazard. Mater. 407 (2021), 124816.
[6] N.J. Jiang, R. Liu, Y.-J. Du, Y.-Z. Bi, Microbial induced carbonate precipitation for immobilizing Pb contaminants: toxic effects on bacterial activity and immobilization efficiency, Sci. Total Environ. 672 (2019) 722–731.
[7] P. Goyal, C.S. Tiwary, S.K. Misra, Ion exchange based approach for rapid and selective Pb(II) removal using iron oxide decorated metal organic framework hybrid, J. Environ. Manag. 277 (2021), 111469.
[8] M. Mao, T. Yan, G. Chen, J. Zhang, L. Shi, D. Zhang, Selective capacitive removal of Pb^{2+} from wastewater over redox-active electrodes, Environ. Sci. Technol. 55 (2021) 730–737.
[9] Z. Wang, Q. Tu, A. Sim, J. Yu, Y. Duan, S. Poon, B. Liu, Q. Han, J.J. Urban, D. Sedlak, B. Mi, Superselective removal of lead from water by two-dimensional MoS_2 nanosheets and layer-stacked membranes, Environ. Sci. Technol. 54 (2020) 12602–12611.
[10] Z. Lu, W. Chu, R. Tan, S. Tang, F. Xu, W. Song, J. Zhao, Facile synthesis of β-$SrHPO_4$ with wide applications in the effective removal of Pb^{2+} and methyl blue, J. Chem. Eng. Data 62 (2017) 3501–3511.
[11] A. Khatoon, R.A.K. Rao, Efficient Cu(II) adsorption from aqueous medium using organic-inorganic nanocomposite material, Groundw. Sustain. Dev. 9 (2019), 100214.
[12] S.M. Husnain, U. Asim, A. Yaqub, F. Shahzad, N. Abbas, Recent trends of MnO_2-derived adsorbents for water treatment: a review, New J. Chem. 44 (2020) 6096–6120.
[13] J. Wang, W. Wang, Z. Ai, M. Li, H. Li, W. Peng, Y. Zhao, S. Song, Adsorption toward Pb(II) occurring on three-dimensional reticular-structured montmorillonite hydrogel surface, Appl. Clay Sci. 210 (2021), 106153.
[14] Z. Wang, J. Xu, D. Yellezuome, R. Liu, Effects of cotton straw-derived biochar under different pyrolysis conditions on Pb (II) adsorption properties in aqueous solutions, J. Anal. Appl. Pyrolysis 157 (2021), 105214.
[15] W. Ahmed, S. Mehmood, A. Núñez-Delgado, S. Ali, M. Qaswar, A. Shakoor, M. Mahmood, D.Y. Chen, Enhanced adsorption of aqueous Pb(II) by modified biochar produced through pyrolysis of watermelon seeds, Sci. Total Environ. 784 (2021), 147136.
[16] Y. Chen, J. Tang, S. Wang, L. Zhang, Ninhydrin-functionalized chitosan for selective removal of Pb(II) ions: characterization and adsorption performance, Int. J. Biol. Macromol. 177 (2021) 29–39.
[17] B.V. Veenhuyzen, S. Tichapondwa, C. Hörstmann, E. Chirwa, H.G. Brink, High capacity Pb(II) adsorption characteristics onto raw- and chemically activated waste activated sludge, J. Hazard. Mater. 416 (2021), 125943.
[18] C. Wang, G. Lin, Y. Xi, X. Li, Z. Huang, S. Wang, J. Zhao, L. Zhang, Development of mercaptosuccinic anchored MOF through one-step preparation to enhance adsorption capacity and selectivity for Hg(II) and Pb(II), J. Mol. Liq. 317 (2020), 113896.

[19] I. Matsukevich, Y. Lipai, V. Romanovski, Cu/MgO and Ni/MgO composite nanoparticles for fast, high-efficiency adsorption of aqueous lead(II) and chromium (III) ions, J. Mater. Sci. 56 (2021) 5031–5040.
[20] A. Briso, G. Quintana, V. Ide, C. Basualto, L. Molina, G. Montes, F. Valenzuela, Integrated use of magnetic nanostructured calcium silicate hydrate and magnetic manganese dioxide adsorbents for remediation of an acidic mine water, J. Water Proc. Eng. 25 (2018) 247–257.
[21] Z. Zhang, T. Wang, H. Zhang, Y. Liu, B. Xing, Adsorption of Pb(II) and Cd(II) by magnetic activated carbon and its mechanism, Sci. Total Environ. 757 (2021), 143910.
[22] I.F. Nata, D.R. Wicakso, A. Mirwan, C. Irawan, D. Ramadhani, U. Ursulla, Selective adsorption of Pb(II) ion on amine-rich functionalized rice husk magnetic nanoparticle biocomposites in aqueous solution, J. Environ. Chem. Eng. 8 (2020), 104339.
[23] W. Xu, Y. Song, K. Dai, S. Sun, G. Liu, J. Yao, Novel ternary nanohybrids of tetraethylenepentamine and graphene oxide decorated with $MnFe_2O_4$ magnetic nanoparticles for the adsorption of Pb(II), J. Hazard. Mater. 358 (2018) 337–345.
[24] F. Valenzuela, G. Quintana, A. Briso, V. Ide, C. Basualto, J. Gaete, G. Montes, Cu (II), Cd(II), Pb(II) and As(V) adsorption from aqueous solutions using magnetic iron-modified calcium silicate hydrate: adsorption kinetic analysis, J. Water Process Eng. 40 (2021), 101951.
[25] Y. Qi, M. Zhang, L. Qi, Y. Qi, Mechanism for the formation and growth of carbonaceous spheres from sucrose by hydrothermal carbonization, RSC Adv. 6 (2016) 20814–20823.
[26] H. Xu, Y. Liu, H. Liang, C. Gao, J. Qin, L. You, R. Wang, J. Li, S. Yang, Adsorption of Cr(VI) from aqueous solutions using novel activated carbon spheres derived from glucose and sodium dodecylbenzene sulfonate, Sci. Total Environ. 759 (2021), 143457.
[27] H. Xu, J. Jia, Y. Guo, Z. Qu, Y. Liao, J. Xie, W. Shangguan, N. Yan, Design of 3D MnO_2/Carbon sphere composite for the catalytic oxidation and adsorption of elemental mercury, J. Hazard. Mater. 342 (2018) 69–76.
[28] P. Maneechakr, S. Mongkollertlop, Investigation on adsorption behaviors of heavy metal ions (Cd^{2+}, Cr^{3+}, Hg^{2+} and Pb^{2+}) through low-cost/active manganese dioxide-modified magnetic biochar derived from palm kernel cake residue, J. Environ. Chem. Eng. 8 (2020), 104467.
[29] X. Bai, X. Tong, Y. Gao, W. Zhu, C. Fu, J. Ma, T. Tan, C. Wang, Y. Luo, H. Sun, Hierarchical multidimensional MnO_2 via hydrothermal synthesis for high performance supercapacitors, Electrochim. Acta 281 (2018) 525–533.
[30] P. Maneechakr, P. Chaturatphattha, S. Karnjanakom, Adsorption behavior of As(V) from aqueous solution by using Fe^{3+}–MnO_4^--modified activated carbon (*Leucaena leucocephala* (Lam) de Wit), Res. Chem. Intermed. 44 (2018) 7135–7157.
[31] S. Karnjanakom, P. Maneechakr, Adsorption behaviors and capacities of Cr(VI) onto environmentally activated carbon modified by cationic (HDTMA and DDAB) surfactants, J. Mol. Struct. 1186 (2019) 80–90.
[32] P. Maneechakr, S. Karnjanakom, Adsorption behaviour of Fe(II) and Cr(VI) on activated carbon: surface chemistry, isotherm, kinetic and thermodynamic studies, J. Chem. Thermodyn. 106 (2017) 104–112.
[33] F. Cao, J. Shen, PEI-Modified CMKGM/GO porous biocomposite for superior removal of Pb(II), J. Chem. Eng. Data 64 (2019) 5622–5629.
[34] Y. Xie, X. Yuan, Z. Wu, G. Zeng, L. Jiang, X. Peng, Adsorption behavior and mechanism of Mg/Fe layered double hydroxide with Fe_3O_4-carbon spheres on the removal of Pb(II) and Cu(II), J. Colloid Interface Sci. 536 (2019) 440–455.
[35] M. Ghaedi, A. Ansari, F. Bahari, A.M. Ghaedi, A. Vafaei, A hybrid artificial neural network and particle swarm optimization for prediction of removal of hazardous dye brilliant green from aqueous solution using zinc sulfide nanoparticle loaded on activated carbon, Spectrochim. Acta Part A 137 (2015) 1004–1015.
[36] S. Dashamiri, M. Ghaedi, K. Dashtian, M.R. Rahimi, A. Goudarzi, R. Jannesar, Ultrasonic enhancement of the simultaneous removal of quaternary toxic organic dyes by CuO nanoparticles loaded on activated carbon: central composite design, kinetic and isotherm study, Ultrason. Sonochem. 31 (2016) 546–557.
[37] H. Nguyen, C. Lin, S. Han, H. Chao, Efficient removal of copper and lead by Mg/Al layered double hydroxides intercalated with organic acid anions: adsorption kinetics, isotherms, and thermodynamics, Appl. Clay Sci. 154 (2018) 17–27.
[38] Y. Zhang, H. Li, Q. Jiang, S. Jiang, Y. Wang, L. Wang, One-pot synthesis of a novel P-doped ferrihydrite nanoparticles for efficient removal of Pb(II) from aqueous solutions: performance and mechanism, J. Environ. Chem. Eng. 9 (2021), 105721.
[39] M. Thommes, K. Kaneko, A.V. Neimark, J.P. Olivier, F. Rodriguez-Reinoso, J. Rouquerol, K.S.W. Sing, Physisorption of gases, with special reference to the evaluation of surface area and pore size distribution (IUPAC Technical Report), Pure Appl. Chem. 87 (2015) 1051–1069.
[40] M.H. Fatehi, J. Shayegan, M. Zabihi, I. Goodarznia, Functionalized magnetic nanoparticles supported on activated carbon for adsorption of Pb(II) and Cr(VI) ions from saline solutions, J. Environ. Chem. Eng. 5 (2017) 1754–1762.
[41] M.Y. Badi, A. Azari, H. Pasalari, A. Esrafili, M. Farzadkia, Modification of activated carbon with magnetic Fe_3O_4 nanoparticle composite for removal of ceftriaxone from aquatic solutions, J. Mol. Liq. 261 (2018) 146–154.
[42] P. Maneechakr, S. Karnjanakom, Selective conversion of fructose into 5–ethoxymethylfurfural over green catalyst, Res. Chem. Intermed. 45 (2019) 743–756.
[43] N.C. Feng, W. Fan, M.L. Zhu, X.Y. Guo, Adsorption of Cd^{2+} in aqueous solutions using $KMnO_4$-modified activated carbon derived from Astragalus residue, Trans. Nonferrous Met. Soc. China 28 (2018) 794–801.
[44] T.T.V. Tran, S. Kaiprommarat, S. Kongparakul, P. Reubroycharoen, G. Guan, M. H. Nguyen, C. Samart, Green biodiesel production from waste cooking oil using an environmentally benign acid catalyst, Waste Manag. 52 (2016) 367–374.
[45] Y. Wang, C. Lin, X. Liu, W. Ren, X. Huang, M. He, W. Ouyang, Efficient removal of acetochlor pesticide from water using magnetic activated carbon: adsorption performance, mechanism, and regeneration exploration, Sci. Total Environ. 778 (2021), 146353.
[46] X. Zhou, C. Jin, G. Liu, G. Wu, S. Huo, Z. Kong, Functionalized lignin-based magnetic adsorbents with tunable structure for the efficient and selective removal of Pb(II) from aqueous solution, Chem. Eng. J. 420 (2021), 130409.
[47] P. Maneechakr, S. Karnjanakom, Environmental surface chemistries and adsorption behaviors of metal cations (Fe^{3+}, Fe^{2+}, Ca^{2+} and Zn^{2+}) on manganese dioxide-modified green biochar, RSC Adv. 9 (2019) 24074–24086.
[48] S. Kumar, R.R. Nair, P.B. Pillai, S.N. Gupta, M.A. Iyengar, A.K. Sood, Graphene oxide-$MnFe_2O_4$ magnetic nanohybrids for efficient removal of lead and arsenic from water, ACS Appl. Mater. Interfaces 6 (2014) 17426–17436.
[49] P. Maneechakr, S. Karnjanakom, The essential role of Fe(III) ion removal over efficient/ low-cost activated carbon: surface chemistry and adsorption behavior, Res. Chem. Intermed. 45 (2019) 4583–4605.
[50] G. Yuvaraja, Y. Pang, D.Y. Chen, L.J. Kong, S. Mehmood, M.V. Subbaiah, D.S. Rao, C.M. Pavuluri, J.C. Wen, G.M. Reddy, Modification of chitosan macromolecule and its mechanism for the removal of Pb(II) ions from aqueous environment, Int. J. Biol. Macromol. 136 (2019) 177–188.
[51] J. Liang, X. Li, Z. Yu, G. Zeng, Y. Luo, L. Jiang, Z. Yang, Y. Qian, H. Wu, Amorphous MnO_2 modified biochar derived from aerobically composted swine manure for adsorption of Pb(II) and Cd(II), ACS Sustain. Chem. Eng. 5 (2017) 5049–5058.
[52] S. Bo, J. Luo, Q. An, Z. Xiao, H. Wang, W. Cai, S. Zhai, Z. Li, Efficiently selective adsorption of Pb(II) with functionalized alginate-based adsorbent in batch/column systems: mechanism and application simulation, J. Clean. Prod. 250 (2020), 119585.
[53] T. Zeng, Y. Yu, Z. Li, J. Zuo, Z. Kuai, Y. Jin, Y. Wang, A. Wu, C. Peng, 3D MnO_2 nanotubes@reduced graphene oxide hydrogel as reusable adsorbent for the removal of heavy metal ions, Mater. Chem. Phys. 231 (2019) 105–108.
[54] H. He, X. Meng, Q. Yue, W. Yin, Y. Gao, P. Fang, L. Shen, Thiol-ene click chemistry synthesis of a novel magnetic mesoporous silica/chitosan composite for selective Hg(II) capture and high catalytic activity of spent Hg(II) adsorbent, Chem. Eng. J. 405 (2021), 126743.
[55] D.H.K. Reddy, S.K. Lee, Magnetic biochar composite: facile synthesis, characterization, and application for heavy metal removal, Colloids Surf. A 454 (2014) 96–103.
[56] A.G. Karunanayake, O.A. Todd, M. Crowley, L. Ricchetti, C.U.P. Jr, R. Anderson, D. Mohan, T. Mlsna, Lead and cadmium remediation using magnetized and nonmagnetized biochar from Douglas fir, Chem. Eng. J. 331 (2018) 480–491.
[57] D. Mohan, P. Singh, A. Sarswat, P.H. Steele, C.U.P. Jr, Lead sorptive removal using magnetic and nonmagnetic fast pyrolysis energy cane biochars, J. Colloid Interface Sci. 448 (2015) 238–250.
[58] A.A. Edathil, I. Shittu, J.H. Zain, F. Banat, M.A. Haija, Novel magnetic coffee waste nanocomposite as effective bioadsorbent for Pb(II) removal from aqueous solutions, J. Environ. Chem. Eng. 6 (2018) 2390–2400.
[59] X. Guo, B. Du, Q. Wei, J. Yang, L. Hu, L. Yan, W. Xu, Synthesis of amino functionalized magnetic graphenes composite material and its application to remove Cr(VI), Pb(II), Hg(II), Cd(II) and Ni(II) from contaminated water, J. Hazard. Mater. 278 (2014) 211–220.
[60] X. Zhang, Y. Li, Yi Hou, Preparation of magnetic polyethylenimine lignin and its adsorption of Pb(II, Int. J. Biol. Macromol. 141 (2019) 1102–1110.
[61] Y. Meng, C. Li, X. Liu, J. Lu, Yi Cheng, L.-P. Xiao, H. Wang, Preparation of magnetic hydrogel microspheres of lignin derivate for application in water, Sci. Total Environ. 685 (2019) 847–855.
[62] M. Li, D. Wei, T. Liu, Y. Liu, L. Yan, Q. Wei, B. Du, W. Xu, EDTA functionalized magnetic biochar for Pb(II) removal: adsorption performance, mechanism and SVM model prediction, Sep. Purif. Technol. 227 (2019), 115696.
[63] K. Chen, J. He, Y. Li, X. Cai, K. Zhang, T. Liu, Y. Hu, D. Lin, L. Kong, J. Liu, Removal of cadmium and lead ions from water by sulfonated magnetic nanoparticle adsorbents, J. Colloid Interface Sci. 494 (2017) 307–316.
[64] J. Ji, G. Chen, J. Zhao, Preparation and characterization of amino/thiol bifunctionalized magnetic nanoadsorbent and its application in rapid removal of Pb (II) from aqueous system, J. Hazard. Mater. 368 (2019) 255–263.
[65] S. Guo, P. Jiao, Z. Dan, N. Duan, J. Zhang, G. Chen, W. Gao, Synthesis of magnetic bioadsorbent for adsorption of Zn(II), Cd(II) and Pb(II) ions from aqueous solution, Chem. Eng. Res. Des. 126 (2017) 217–231.
[66] P. Roy, N.K. Mondal, K. Das, Modeling of the adsorptive removal of arsenic: A statistical approach, J. Environ. Chem. Eng. 2 (2014) 585–597.
[67] Y. Niu, X. Han, L. Huang, J. Song, Methylene blue and lead(II) removal via degradable interpenetrating network hydrogels, J. Chem. Eng. Data 65 (2020) 1954–1967.
[68] Y. Liu, Y. Xiong, P. Xu, Y. Pang, C. Du, Enhancement of Pb (II) adsorption by boron doped ordered mesoporous carbon: Isotherm and kinetics modeling, Sci. Total Environ. 708 (2020), 134918.
[69] R. Ahmad, A. Mirza, Synthesis of guar gum/bentonite a novel bionanocomposite Isotherms, kinetics and thermodynamic studies for the removal of Pb(II) and crystal violet dye, J. Mol. Liq. 249 (2018) 805–814.
[70] D. Liu, Y. Tang, J. Li, Z. Hao, J. Zhu, J. Wei, C. Liu, L. Dong, B. Jia, G. Chen, Eupatorium adenophorum derived adsorbent by hydrothermal-assisted HNO_3 modification and application to Pb^{2+} adsorption, J. Environ. Chem. Eng. 9 (2021), 105972.